Dynamic cutting process modelling and its impact on the generation of surface topography and texture in nano/micro cutting

L Zhou[1,2]* and K Cheng[2]

[1]School of Mechatronics Engineering, Harbin Institute of Technology, Harbin, Heilongjiang, People's Republic of China

[2]School of Engineering and Design, Brunel University, Uxbridge, UK

Abstract: In the nano/micro cutting process, the surface quality is heavily dependent on all the dynamic factors, including those from the material, tooling, process parameters, servo accuracy, mechanical structural stiffness, and non-linear factors as well. The machined surface is generated based on the tool profile and the real tool path combining with the various external and internal disturbances. To bridge the gap between the cutting process and the surface topography/texture generation, an integrated simulation-based approach is presented involving the dynamic cutting process, control/drive system, and the surface generation. The simulations take account of all the intricate aspects of the cutting process resulting in the surface topography and texture formation, such as material heterogeneity, regenerative chatter, built-up edge (BUE), tool wear, spindle runout, environmental vibration, tool interference, etc. Both the frequency ratio method and sampling theorem are used to interpret the surface topography and texture formation. The effects of non-linear factors on the surface generation are simulated and analysed through the power spectral density (PSD) and significance on surface texture. The relationships among cutting force, tool path, and surface profile are discussed in detail. Furthermore, the proposed systematic modelling approach is verified by cutting trials, which provide the coincident results of the surface topography and areal power spectral density (APSD).

Keywords: dynamic cutting force, surface topography, surface texture, tool interference, APSD, significance analysis

1 INTRODUCTION

Metal cutting at the nano/micro scale is a complex process that comprises the workpiece material, tooling geometry, cutting process parameters, servo drive accuracy, static and dynamic deformations of the machine structure, etc. The machined surface is generated based on the tool profile and real tool path considered with various disturbances. It is of great benefit to develop a systematic model and analyse the effects from the dynamic cutting process. Many linear/non-linear factors in the whole system will contribute to the surface topography and texture formation, such as material heterogeneity [1, 2], chatter [3], built-up edge (BUE) [4], tool wear [5], spindle runout [6], environmental vibration, etc. The dynamic cutting force reflects the collective effects of all the factors above, and leads to the tool–workpiece relative displacement in the stiffness loop. Therefore, the investigation on the dynamic cutting force modelling and its impact is essential and much needed, particularly in a scientific and analytical manner.

Taking the three-axis turning machine as a case study in point, as shown in Fig. 1, the stiffness loop in the face cutting process involves:

(a) spindle axial runout,
(b) workpiece clamp error,
(c) workpiece material property,

*Corresponding author: School of Mechatronics Engineering, Harbin Institute of Technology, New Technology Building, No 92, West Da Zhi Street, Harbin, Heilongjiang 150001, People's Republic of China. email: zhoulei201hit@163.com
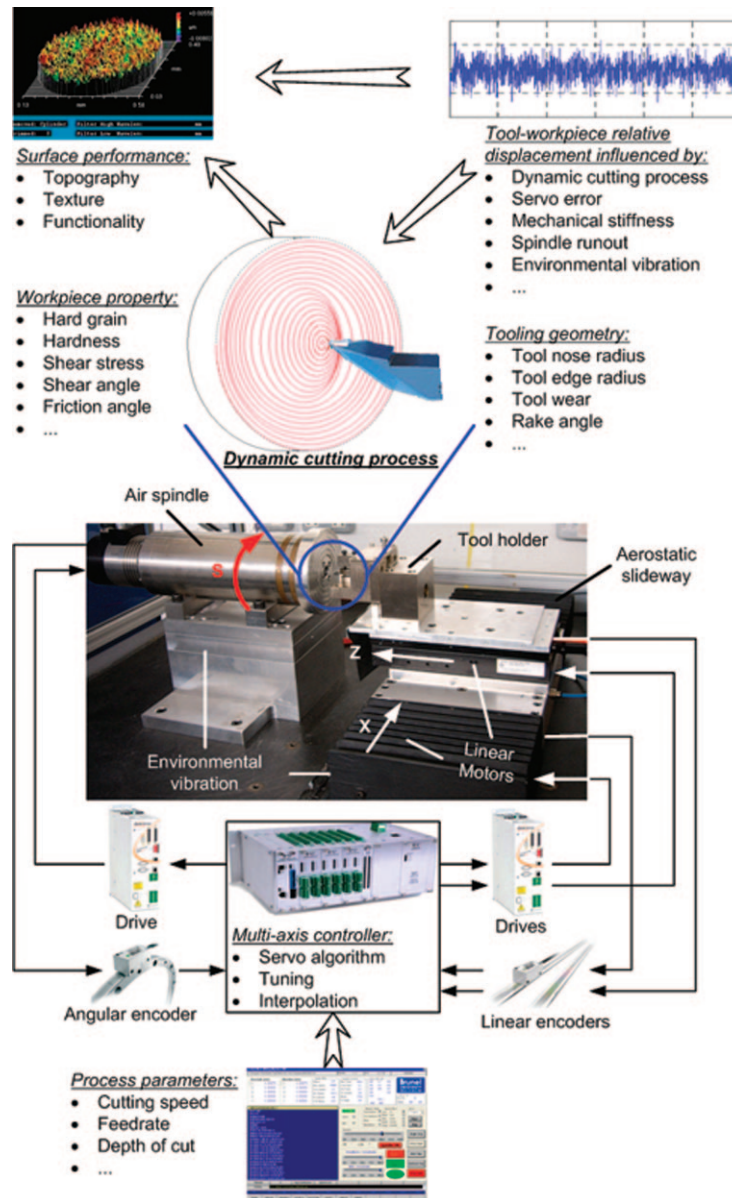
Fig. 1 The machine control loop and stiffness loop in nano/micro cutting

(d) cutting tool geometry,
(e) tool holder stiffness,
(f) Z axis servo stiffness in the axial direction,
(g) X axis slideway stiffness in the side direction,
(h) mounting stiffness.

In the nano/micro cutting process, the surface performance of undertaking the high-precision machining is all about how the tool–workpiece relative position rightly maintains its desired objective. In the machine stiffness loop, all the elements are guaranteed by physical construction like bearings, mounting screws, and other mechanical structures except the linear motor in the axial direction. Since employing the direct driven linear motor, the stiffness in Z axial motion is directly provided by the electrical servo motor. The tuning of the Z axis linear motor, which is in the error-sensitive direction, is therefore one of the most critical ingredients of design and uses the ultra-precision machine tool.

The topography and texture of the machined surface are generated by the dynamic feed response under the multifarious cutting factors. Several literatures focus on the surface topography generation process in relation to getting the connection of the tool path and the machined surface. Cheung and Lee [7–9] and Kim et al. [10] used the digitizing oscilloscope to record the relative displacement between the cutting tool and the workpiece surface. After being analysed by fast Fourier transform (FFT), the main frequency and amplitude of the vibration reconstructs the tool deviation from the ideal position. The tool

Proc. IMechE Vol. 223 Part B: J. Engineering Manufacture

JEM1316 © IMechE 2009

profile superimposes on to the tool path to generate the surface topography. Lee and Cheung and colleagues [11, 12] developed a dynamic cutting system to predict the surface topography in face turning. However, the cutting force model only contains the linear factors, and the whole response system was simplified into a second-order system. In fact, the advanced control algorithms are always applied to ultra-precision machine tools so as to achieve a higher servo performance. Using a second-order system may marginally succeed in traditional machine tools, but it loses the modelling accuracy in ultra-precision machines. The servo control system, material hard grain effect, chatter, tool wear, spindle runout, and environmental vibration were also not taken into account in these papers. Luo *et al.* [13, 14] introduced some non-linear factors into the cutting process and continued to use a second-order response system. Furthermore, the effect of non-linear factors on the surface generation had not been involved.

For the generation algorithm of the machined surface, the most important procedure is to get the correct remaining profiles. The traditional approaches [8–13] compute the intersection of two adjacent tool profiles in order to get each tool profile boundary. However, single-point diamond turning, which is under a finer feed rate, a larger tool nose radius, a higher spindle rotational speed, and a greater unit cutting force, will be more susceptible to the effect of the tool interference [7, 15]. The computation of remaining profiles on the machined surface should be based on not only the neighbouring tool profiles but also all the profiles that might intersect and overcut the previous tool marks because of the tool interference effect.

In this paper, the following novel work is presented, including:

1. To develop the control/drive system model into the systematic prediction model of the surfaces in face turning.

2. To include the non-linear factors into the dynamic cutting model to simulate the real dynamic cutting process and study the significance of the factors on surface quality.
3. To produce a surface generation algorithm in consideration of the tool interference effect.
4. To elucidate the formation of the flutes/rings on the machined surface and find out the error origins of the dynamic cutting factors through the power spectral density (PSD) analysis.

2 SYSTEMATIC MODELLING OF THE DYNAMIC NANO/MICRO CUTTING

As illustrated in Fig. 2, the generation of the workpiece surface in nano/micro cutting is a very complex material removal process, including:

(a) servo control dynamics, which is dependent on control algorithms, servo amplifiers, actuators, and inspection sensors;
(b) machining process dynamics, which is heavily affected by the machine tool performance, tooling geometry, workpiece material properties, operation factors, servo motion, and working environment;
(c) surface generation and surface analysis on its texture, integrity, and functionality.

To obtain a better understanding of this complex process, a systematic model is developed in the MATLAB Simulink module, as shown in Fig. 3. The modelling approach bridges the gap between the determinative factors and the surface generation. Based on a thorough theoretical analysis of servo motions and cutting mechanics and dynamics, the integrated model produces a scientific methodology to simulate the precision surface generation in nano/micro turning processes.
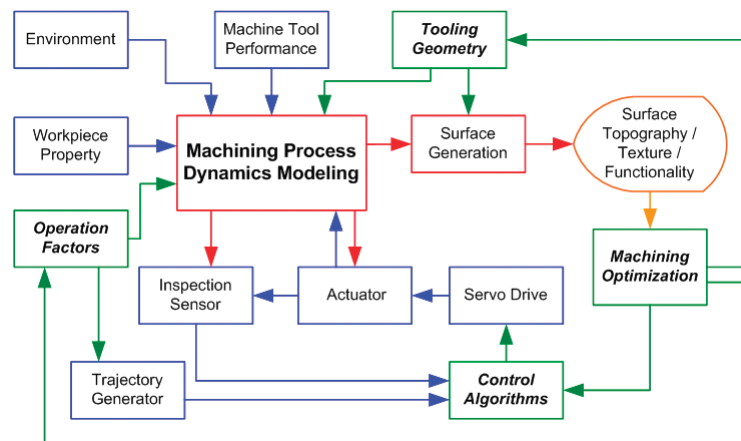

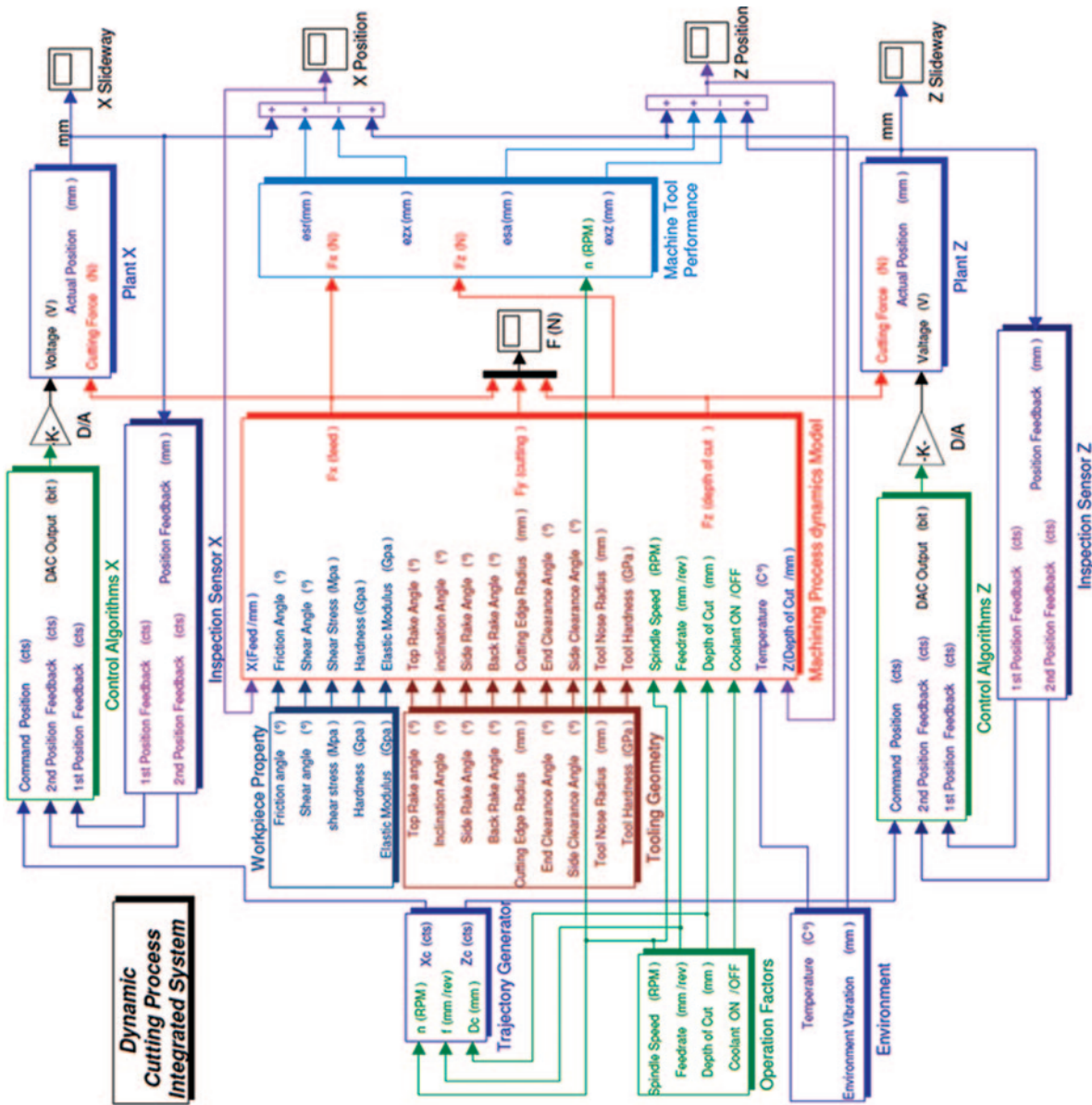**Fig. 2** An illustration of the machining process integration system

Fig. 3 Integrated modelling of the dynamic cutting process

2.1 Modelling of servo control dynamics

Most of the simulations on cutting dynamics are simplified by modelling the control and drive system as a second-order system. However, the details in the servo control system cannot be neglected. In this paper, the ultra-precision turning machine presented employs the UMAC motion controller, which provides a proportional-integral-derivative (PID) position/velocity servo control scheme with velocity and acceleration feedforward loops as shown by [16]

$$\text{DAC}_{\text{out}} = 2^{-19} K_{\text{p}} \left[K_{\text{sp}} \left(FE + \frac{K_{\text{vff}} CV + K_{\text{aff}} CA}{128} + \frac{K_{\text{i}} IE}{2^{23}} \right) - \frac{K_{\text{d}} K_{\text{sv}} AV}{128} \right] \tag{1}$$

A PID loop with feedforward compensation is used to control all the machine axes. The feedforward assists in eliminating most of the time delay between commanded and actual positions. In other words, it reduces the phase lag in the system. An augmentable first-order lowpass filter helps to attenuate the quantization noise, particularly when higher bandwidths are required.

The block diagram in Fig. 4 strictly follows equation (1) to simulate the real controller activities. The discrete model uses Z-transforms whose sampling period is the real servo interrupt cycle. The position quantification based on the encoder resolution is 4.88 nm. A linear compensation function counteracts the friction from the physical plant according to the velocity direction.

The output from the UMAC controller is led to the servo amplifier to continue the current loop, as shown in Fig. 5. The direct-drive linear motor model is built on the resistance and inductance of the motor windings, force constant, and the back electromotive force (EMF) constant from the specifications. In this case, the aerostatic bearing slideway is applied to reduce the friction and unexpected load in the motion direction. Therefore, the plant of the slide carriage is simplified to represent a pure mass module.

From the servo control dynamics model, the actual motion of each slideway is calculated for the next stage to generate the real tool path. In fact, there are some additional disturbances in the drive system, such as the cutting force disturbance superimposed on the slideways, which is generated by the dynamic cutting process.

2.2 Dynamic cutting process

The quality of the machined surface is mainly determined by the relative motions between the cutting tool edge and the workpiece. In practice, the tool path deviates from the ideal tool path as a result of kinematic or dynamic factors from the dynamic cutting process, machine tool motion errors, and environmental disturbances. For instance, the deformation of the aerostatic slideway under the action of dynamic cutting forces will deflect the cutting tool nose point; environmental vibrations will move the motion of the cutting tool away from the designed tool path.

Since the surface topography model basically follows the reflection of the cutting tool edge profile, the calculation of the real tool path becomes the critical part in the modelling approach. Table 1 lists the linear and non-linear factors from the structural deformation and motion errors of the machine tool and cutting tool, which will contribute to the deviation of the tool path.

All the cutting process dynamics related to functions above are modelled as illustrated in Fig. 6. In the same way, the motion errors of the machine tool presented in Fig. 3 are superimposed on the output of the slideways to generate the real tool path.

As demonstration workpiece material is aluminium alloy, the dynamic cutting force model will thus follow the elastic–plastic mechanics model. According to the elastic–plastic deformation principle, the forces acting on the tool rake face can be acquired by the coordinate transformation of the shear plane force based on the shear plane cutting model. The force acting on the tool cutting edge and flank face can be deduced based on the empirical formula of the contact stress and elastic recovery. Accumulating the forces' action on the three zones, there will be the dynamic cutting forces in the three directions, following the Cartesian coordinate system in Fig. 1, expressed as [19, 20]

$$F_x(t) = (K_{\text{fc}} - K_{\text{rc}}) \sin \theta_{\text{r}} (d_{\text{c}} + \Delta c_{\text{t}}) \left[(h + \Delta c_{\text{w}}) + \sqrt{R_0^2 - (R_0 - d_{\text{c}} - \Delta c_{\text{t}})^2} \right] + K_{\text{re}} R_0 \theta_{\text{r}} \sin \theta_{\text{r}}$$

$$F_y(t) = K_{\text{tc}} (d_{\text{c}} + \Delta c_{\text{t}}) \left[(h + \Delta c_{\text{w}}) + \sqrt{R_0^2 - (R_0 - d_{\text{c}} - \Delta c_{\text{t}})^2} \right]$$

$$+ K_{\text{te}} R_0 \theta_{\text{r}} + K_{\text{ff1}} \left(\sin \frac{\beta}{2} - \mu \cos \frac{\beta}{2} \right) + K_{\text{ff2}} (\sin \beta - \mu \cos \beta)$$

$$F_z(t) = (K_{\text{fc}} \sin \theta_{\text{r}} + 1 - \cos \theta_{\text{r}}) (d_{\text{c}} + \Delta c_{\text{t}}) \left[(h + \Delta c_{\text{w}}) + \sqrt{R_0^2 - (R_0 - d_{\text{c}} - \Delta c_{\text{t}})^2} \right]$$

$$+ (K_{\text{fe}} \sin \theta_{\text{r}} + 1 - \cos \theta_{\text{r}}) R_0 \theta_{\text{r}} + K_{\text{ff1}} \left(\cos \frac{\beta}{2} + \mu \sin \frac{\beta}{2} \right) + K_{\text{ff2}} (\cos \beta + \mu \sin \beta) \tag{10}$$
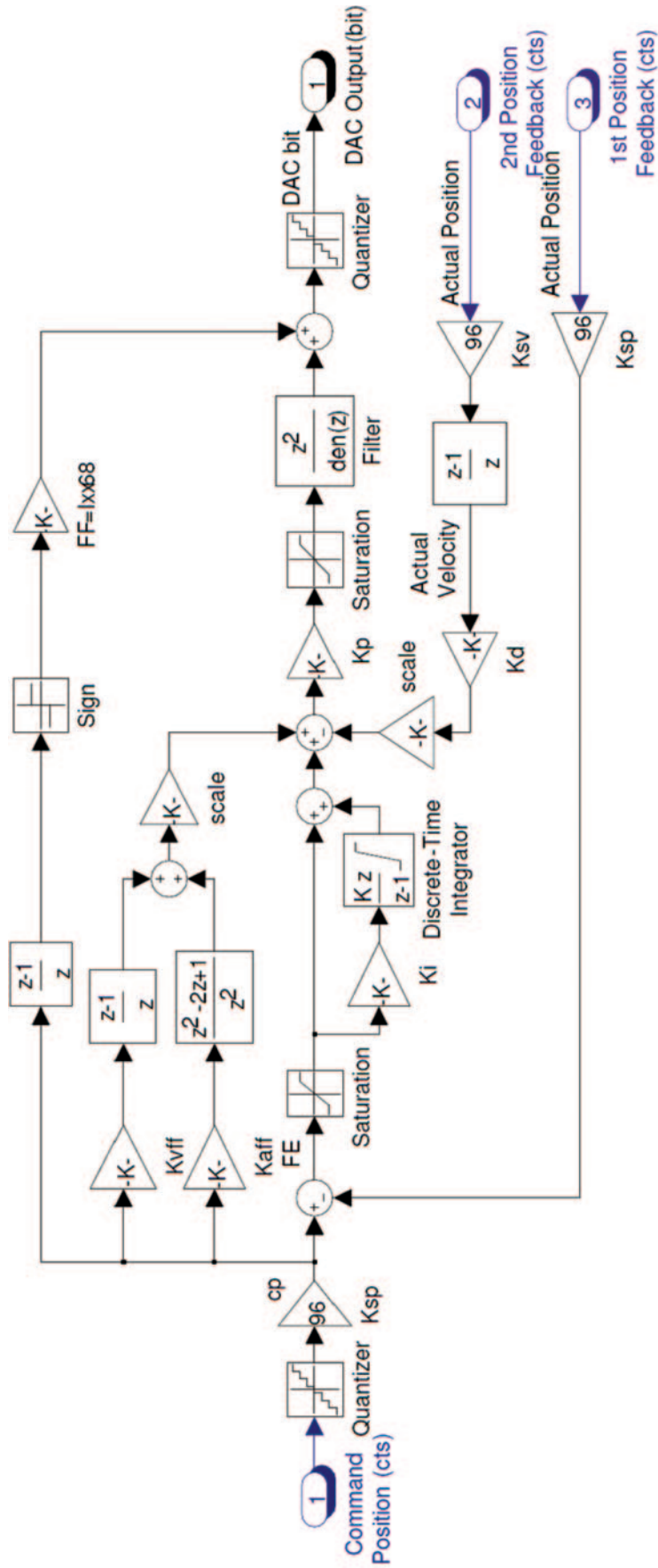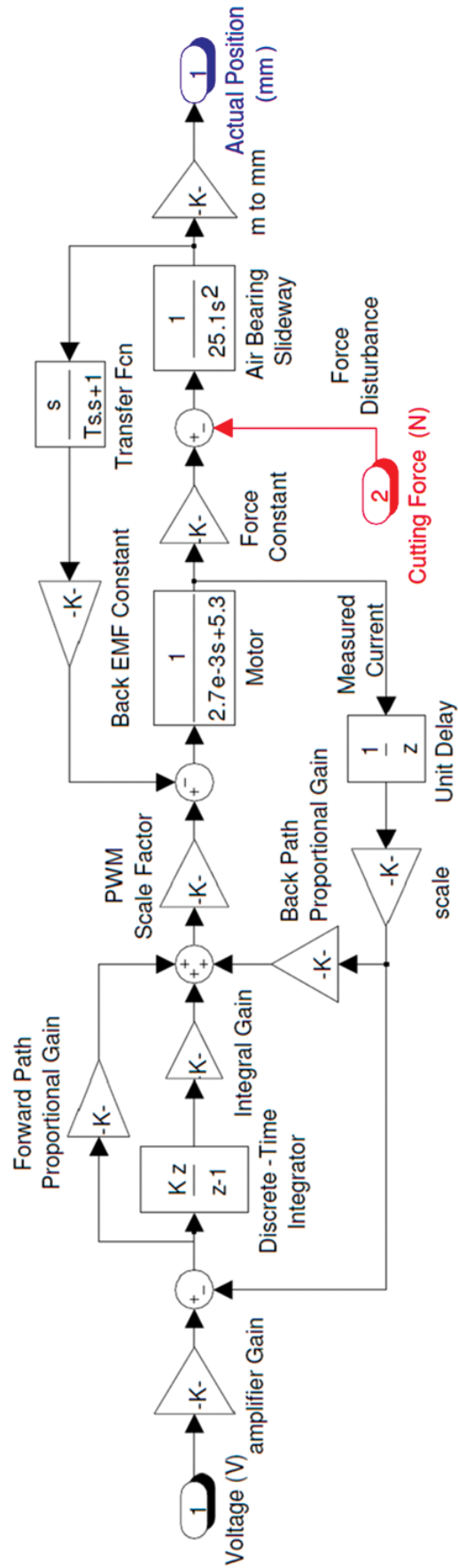
Fig. 4 Servo controller model

Fig. 5 Drive system model

Table 1 Linear and non-linear factors in the cutting process

Source	Influence factor	Mathematical function	
BUE	Rake angle	$\Delta\alpha = \alpha_A \, \mathrm{Saw}\,(\omega_\alpha t)$	(2)
Hard grain	Shear stress and hardness of workpiece	$\Delta\tau = A_\tau \, \mathrm{Pul}(t)$ $\Delta H = A_H \, \mathrm{Pul}(t)$	(3)
Shear angle oscillation	Shear angle	$\Delta u = A_u \sin(2\pi f_u t)$	(4)
Flank wear	Tool wear	$l_w = \frac{A}{H_t}\frac{F_s}{Vf}V_s + B \exp\left(\frac{-E}{RT_f}\right)$ [17, 18]	(5)
Regenerative vibration	Feed and depth of cut chatter	$\Delta c_t = z(t) - z(t - T)$ $\Delta c_w = x(t) - x(t - T)$	(6)
Spindle runout	Displacement between the cutting tool and the workpiece	$e_{sr} = A_{sr}\sin(\omega t + \phi_r)$ $e_{sa} = A_{sa}\sin(\omega t + \phi a)$	(7)
Slideway stiffness		$e_{zx} = F_x/K_{zx}$ $e_{xz} = F_z/K_{xz}$	(8)
Environmental vibration		$e_{vx} = A_{evx}\sin(2\pi f_{ev}t)$ $e_{vz} = A_{evz}\sin(2\pi f_{ev}t)$	(9)

As described, the real tool path is created by all the above factors, including servo motions influenced by dynamic cutting disturbance, machine tool deformations, and environmental vibrations. Therefore, it is expressed as

$$x_{tp} = x_{sm} + e_{evx} + e_{sr} - F_x/K_{zx}$$
$$z_{tp} = z_{sm} + e_{evz} + e_{sa} - F_z/K_{xz}$$
(11)

3 SIMULATION OF NANO/MICRO MACHINED SURFACES

3.1 Prediction algorithms for a machined surface

The ultimate stage of the machining system is to render the surface topography. The cutting tool will follow the real tool path to reproduce the tool profile on the machined surface in the form of feed marks, as illustrated in Fig. 7.

The traditional surface generation algorithms [8–13] calculate the intersection of two adjacent tool profiles to get the boundary of each feed mark, as in Fig. 8(a). However, in the ultra-precision machining, the feedrate is so small that the next several cuts will clean up the previous tool marks when there are vibrations in motion. As shown in Fig. 8(b), the $(i+1)$th and $(i+2)$th tool profiles, which are overcut by the $(i+3)$th, cannot affect the workpiece surface generation. The machined surface is contoured by the ith, $(i+3)$th, $(i+4)$th, etc. tool profiles as a result of tool interference from vibrations. Generally speaking, the vibration of the tool path is not the entire reason

for forming the surface topography. The tool interference appears normally in the cutting process with a small feedrate, which always helps to filter out the tool–workpiece vibration and form a more complex surface topography.

To simulate the three-dimensional surface topography, the surface is sampled into a finite number of equally spaced radial sections. The number of sections, N_s, can be expressed as

$$N_s = 2\pi/\Delta\theta$$
(12)

and the number of spindle rotation rounds during machining, N_r, can be calculated as

$$N_r = R_w/f$$
(13)

Therefore, the total simulation points are

$$N_p = N_s N_r + 1$$
(14)

The dynamic cutting process model outputs x_{tp} and z_{tp} to form the real tool path as the ultimate result. In the face-turning situation with cylindrical coordinates, x_{tp} is actually the radius of the tool nose point and z_{tp} the amplitude correspondingly. To convert the three-dimensional tool path into a rectangular coordinate system, there are

$$x_c = x_{tp}\cos(p\,\Delta\theta)$$
$$y_c = x_{tp}\sin(p\,\Delta\theta) \qquad (p = 1, 2, \ldots, N_p)$$
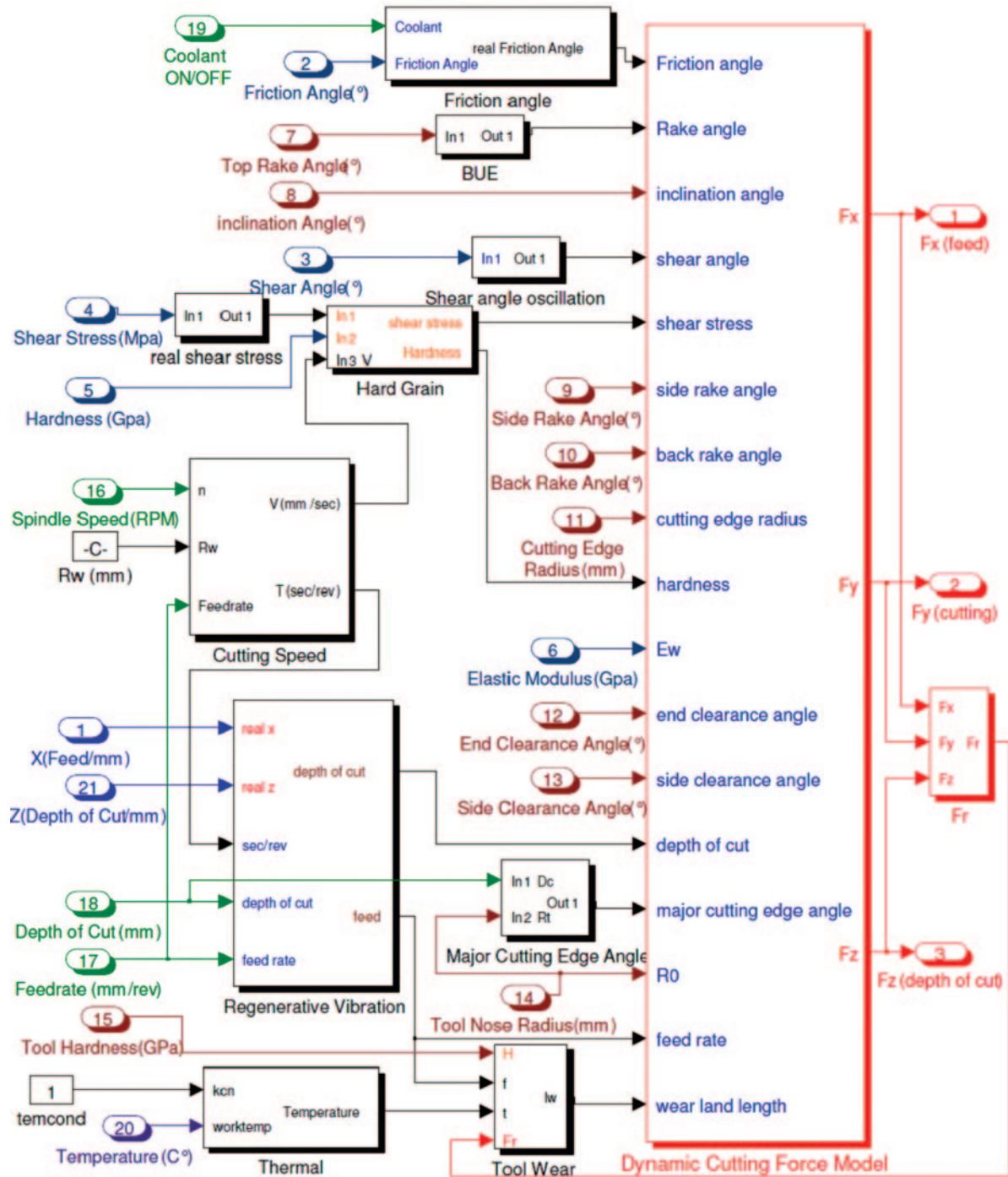$$z_c = z_{tp}$$

(15)

Fig. 6 Cutting process dynamics model

As shown in Fig. 8, tool profiles in each radial section may interfere with the earlier ones. For this reason, it is better to calculate all the tool profiles according to the tool nose points and maintain the lowest curves. At the jth radial section, the tool nose point in the polar coordination form can be described as

$$\theta_a(i,j) = (j-1)\Delta\theta$$
$$r_a(i,j) = x_{tp}[(i-1)N_s + j]$$
$$h_a(i,j) = z_{tp}[(i-1)N_s + j]$$
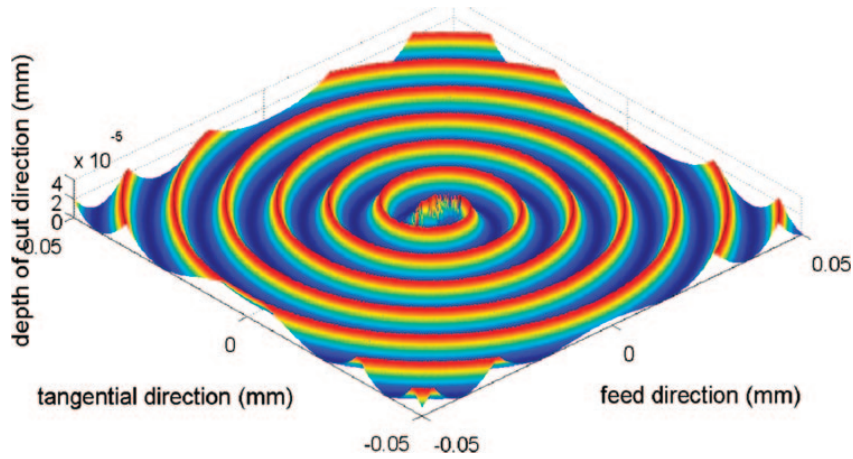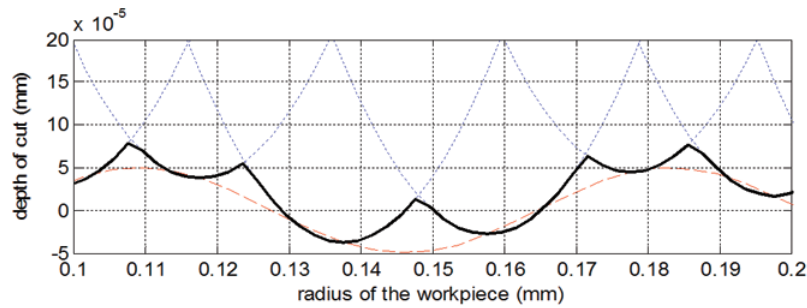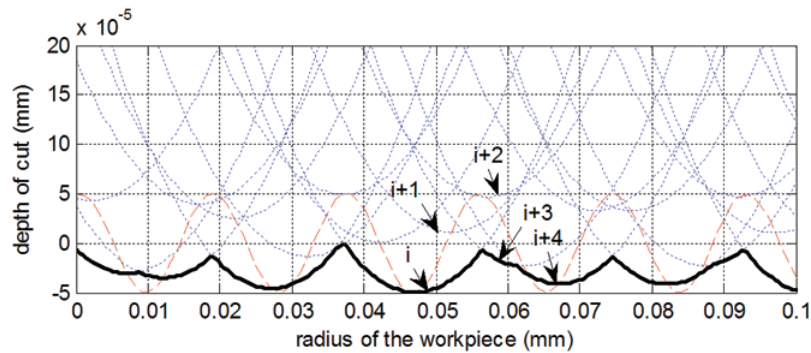$$i = 1, 2, \ldots, N_r; \qquad j = 1, 2, \ldots, N_s$$

(16)

Fig. 7 Simulation of feed marks on the machined surface

(a) Intersections of two adjacent tool profiles

(b) Intersections in consideration of all tool profiles

Fig. 8 Simulations on the two-dimensional machined surface profiles

To superpose the tool profiles on to the tool nose points, the sampling points at the jth radial section should be refined by Δf, which is smaller than f to shape the tool edge. Setting the tool nose radius as R_0

$$\theta_t(k, i, j) = (j - 1)\Delta\theta$$
$$r_t(k, i, j) = r_a(i, j) + k\Delta f$$
$$h_t(k, i, j) = h_a(i, j) + \left[R_0 - \sqrt{R_0^2 - (k\Delta f)^2} \right]$$
$$-\frac{L_t}{2\Delta f} \leqslant k < \frac{L_t}{2\Delta f}$$

(17)

and the tool projected length in the X direction as L_t, the height of the surface point at the (i, j) point is geometrically determined as

Comparing all the tool edge profiles with the depth of cut d_c, it is easy to get the residual contour while the relevant radius is calculated by the linear interpolation method, i.e. there is

$$\theta(l, j) = (j - 1)\Delta\theta$$
$$r(l, j) = r_a(i, j) + (l - if/\Delta f)[r_a(i + 1, j) - r_a(i, j)]$$
$$h(l, j) = \min[h_t(k, i, j), d_c]$$
$$l = 1, 2, \ldots, R_w/\Delta f$$

(18)

Transforming the polar coordinates to Cartesian ones, the three-dimensional surface topography is expressed as

$$\begin{aligned} x &= r\cos(\theta) \\ y &= r\sin(\theta) \\ z &= h \end{aligned} \tag{19}$$

All the three-dimensional surface topography prediction procedures are described as a block flow diagram in Fig. 9. The principal advantage of this approach is in considering multiple tool interference, which is more consistent than the real practice.

3.2 Simulation on the surface generation

The relative displacement between the tool and the workpiece in the Z direction is mainly decided by the workpiece material, machine tool performance, tooling geometry, and cutting parameters, which are listed in Table 2. The simulated surface, cut from the edge to the centre of the workpiece, is a 1.4 mm $\times$ 1.4 mm square located at the spindle central line, as shown in Fig. 10.

The impressive features on the surfaces are the rings and flutes, which are much bigger than the tool feed mark size. To analyse the waviness structure regulation, it is essential to work out the intrinsic connection between the vibrations and the machined surface topography.

Since the tool paths in one section are the discrete points by feed spacing per spindle revolution, the surface generation acts as the process of the cutting tool edge sampling the vibratory tool path in the feed direction. The machined surface topography under vibration is directly determined by the relation between the vibration frequency f_v and the spindle rotational frequency f_s, i.e. their ratio f_r is

$$f_r = \frac{f_v}{f_s} = \frac{f_v}{n/60} = a + b \tag{20}$$

In this case namely, f_r is the frequency that the tool tip traverses the vibration within one spindle rotation period. The number of flutes is identical to the integer a, which is the number of times the vibration is completely undergone per spindle revolution. The absolute fractional value $|b|$, which cannot cover the full vibration cycle, will make the phase offset in each spindle rotation. The orientation of the flutes is decided by the sign of b. A positive sign means counterclockwise and a negative sign is clockwise in this case. In other words, the radial section represents the fractional part b of the frequency ratio, while the integer a will be reflected in the circumferential direction.

4 SIMULATION RESULT ANALYSIS

As described in section 3, the machined surface generation can be geometrically thought of as a result of transferring the tool profile on to the workpiece. To explore the surface topography and texture characteristic further, it is essential to find out the source causing the tool–workpiece relative deflection.

4.1 Power spectral analysis

The fast Fourier transform (FFT) function is extensively used to study the frequency components of a signal buried in a noisy time domain signal. The power spectral density (PSD) is intended for discrete spectra computation with the FFT algorithm. The integral of the PSD over a given frequency band computes the average power in the signal in that frequency band. The peak of the PSD at a given frequency reflects the power per unit frequency. In other words, the signal's frequency contents and their distribution at the frequency can be directly perceived through the PSD analysis.

From the PSD of F_z in Fig. 11, it is found that the cutting force in the Z direction is mainly focused on 25 Hz (BUE), 32 Hz (hard grain), 45 Hz (shear angle oscillation), and their high-order harmonic components. From the amplitudes of the PSD, the most contributions in power are clearly from workpiece material properties in contrast with the others from the cutting process.

It is shown in Fig. 12 that all the frequency components of the cutting force clearly remain on the tool–workpiece relative displacement in the dynamic cutting process. The differences in the PSD from F_z are an additional 3.47 Hz (environmental vibration) and 16.67 Hz (spindle runout). The cutting force disturbance will be rejected by the servo motor and bearings on the slideway. From Fig. 12, even with the small force turbulence, the direct drive system will lose much accuracy. To improve the resistance of the disturbance, it is better to increase the damping of the servo control system and the physical stiffness and damping of slideways.

Figure 13 presents the tool path, tool profiles, and the final resultant surface topography in one section. When converting the tool path into the surface topography, the temporal frequency f_v (Hz) should also be converted to the spatial frequency f_{vs} (mm^{-1}) as

$$f_{vs} = \frac{f_v}{f_s f} \tag{21}$$

Accordingly, the key frequencies in the tool path of 3.5, 16.7, 25, 32, 45, 64, and 96 Hz will be equal to 21, 100, 150, 192, 270, 384, and 576 mm^{-1}. In the light of
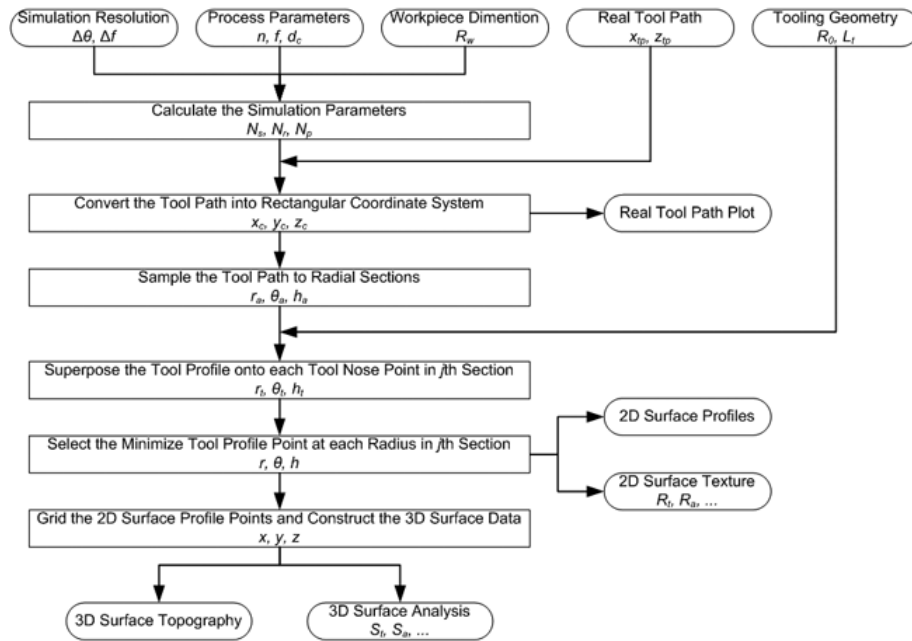
Fig. 9 A flowchart of the simulation model to predict the three-dimensional machined surface topography

Table 2   Simulation conditions for face turning

|	Factors	Frequency	Amplitude	Function
Workpiece material	BUE	25 Hz	2°	Sawtooth wave
(Aluminium 6061)				
	Hard grain – shear stress	32 Hz	30 MPa	Square wave
	– hardness	32 Hz	0.1 GPa	Square wave
	Shear angle oscillation	45 Hz	2°	Sine wave
Machine tool	Environmental vibration	3.5 Hz	10 nm	Sine wave
performance	Spindle axial runout	16.67 Hz	20 nm	Sine wave
	Slideway side stiffness	—	40 N/μm	—
Tooling geometry	Tool nose radius	—	0.508 mm	—
	Cutting edge radius	—	50 nm	—
	Top rake angle	—	− 2.5°	—
Cutting parameters	Spindle rotational speed	—	1000 r/min	—
	Feedrate	—	0.01 mm/rev	—
	Depth of cut	—	0.01 mm	—
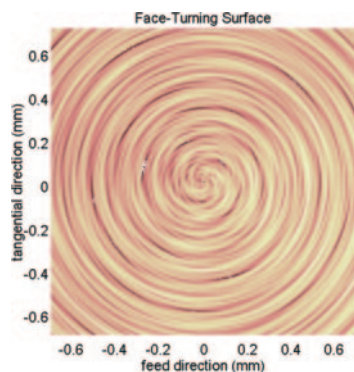
Fig. 10   Simulation on the face turning surface

equations (20) and (21), $|b|$ in the ascending sort is 0.08, 0.16, 0.21, 0.24, 0.3, 0.5, and 1, whose corresponding spatial frequencies are 8, 16, 21, 24, 30, 50, and 100 mm^{-1}. The values closely dovetail with the PSD frequencies, as shown in Fig. 13.

Viewing from the frequency domain, the surface topography in one section is sampled by the feeding distance per spindle revolution. In fact, the cutting in the radial section is the process to sample the tool path by the spindle rotational frequency f_s. Since the tool path contains many frequencies exceeding $f_s/2$, the process will not conform to the Nyquist condition of the sampling theorem. Aliasing will occur and the
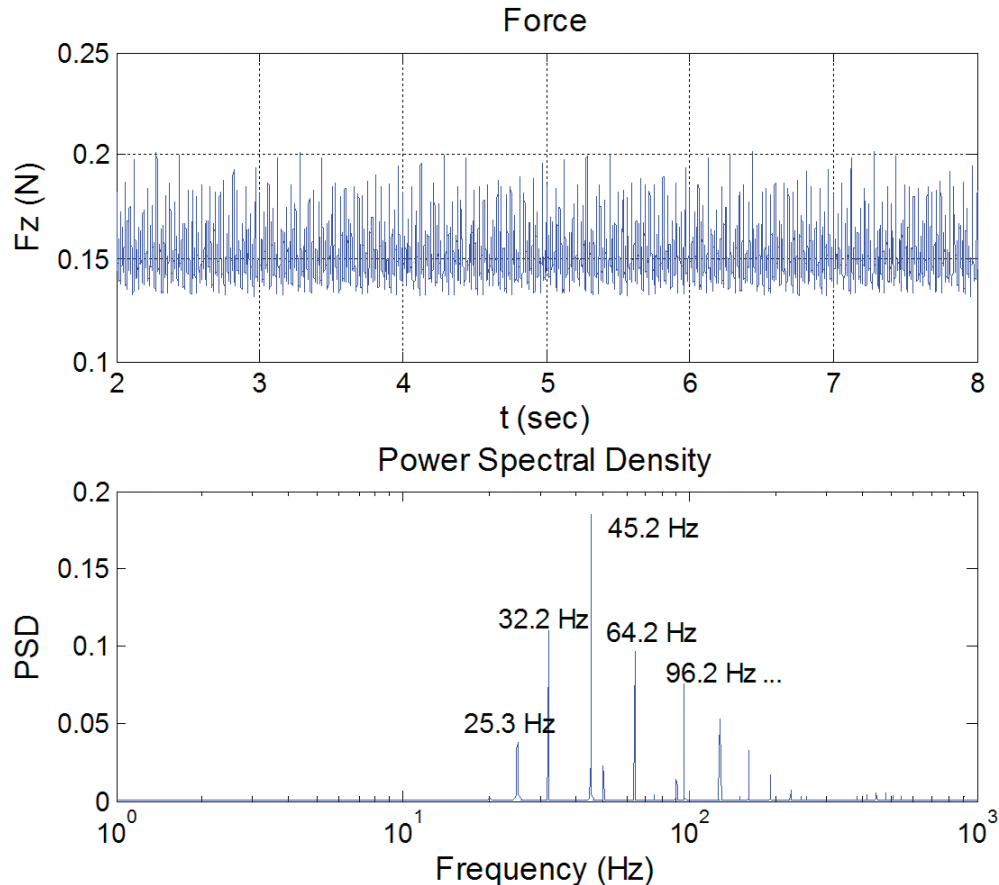
Force

Power Spectral Density

Fig. 11 Cutting force in the Z direction and its PSD

subsampling effect aliases the high-frequency signals into low-frequency ones. On this account, the new frequency spectrum f_p is proposed within one sampling bandwidth $(-f_s/2 < f_p \leqslant f_s/2)$

$$f_p = mf_s - f_v, \frac{f_v}{f_s} - \frac{1}{2} < m \leqslant \frac{f_v}{f_s} + \frac{1}{2} \qquad (22)$$

The sampling method leads to an identical result as to the frequency ratio explained above.

At the same time, the higher frequency vibrations are attenuated rapidly, which means the wavelengths of the waviness produced at the radial sections are all greater than $f/2$. Therefore, the waviness in the radial direction can be controlled by the spindle speed and feed rate.

4.2 Areal power spectral analysis

Although PSD can explain the formation of the surface profile in two dimensions in one radial section, it is incapable of evaluating the whole surface topography. However, the trend in modern advanced manufacturing is to obtain the functionality of a component by the control of three-dimensional topography and texturing. The areal method in three dimensions is much more powerful than the profile method in two dimensions, in that it can be used to characterize functional aspects of a surface topography. Furthermore, it shows the intricate embedded information to how the surface was manufactured.

The areal power spectral density (APSD) is a three-dimensional analysis that renders the information on the overall surface topography. Figure 14 shows the APSD of the face-turning surface which has strong anisotropy in the right-angled axes but obvious isotropy in the polar coordinates. The peaks are distributed on specific frequency rings, which are identical to those on the previous PSD components. The sections on the same radius point out the number of flutes on the machined surface. In other words, the number of sections in APSD is represented as m (or a), as explained before, and the radius states the spatial frequency f_p (or b). Taking the $50 \, \text{mm}^{-1}$ ring as an example, the ring is separated into four centre-symmetric sections. Owing to the dual symmetry of the APSD function, the four peaks give $m = 2$. Therefore, the original vibration should be $150 \, \text{mm}^{-1}$, which comes from a 25 Hz BUE triangular wave.
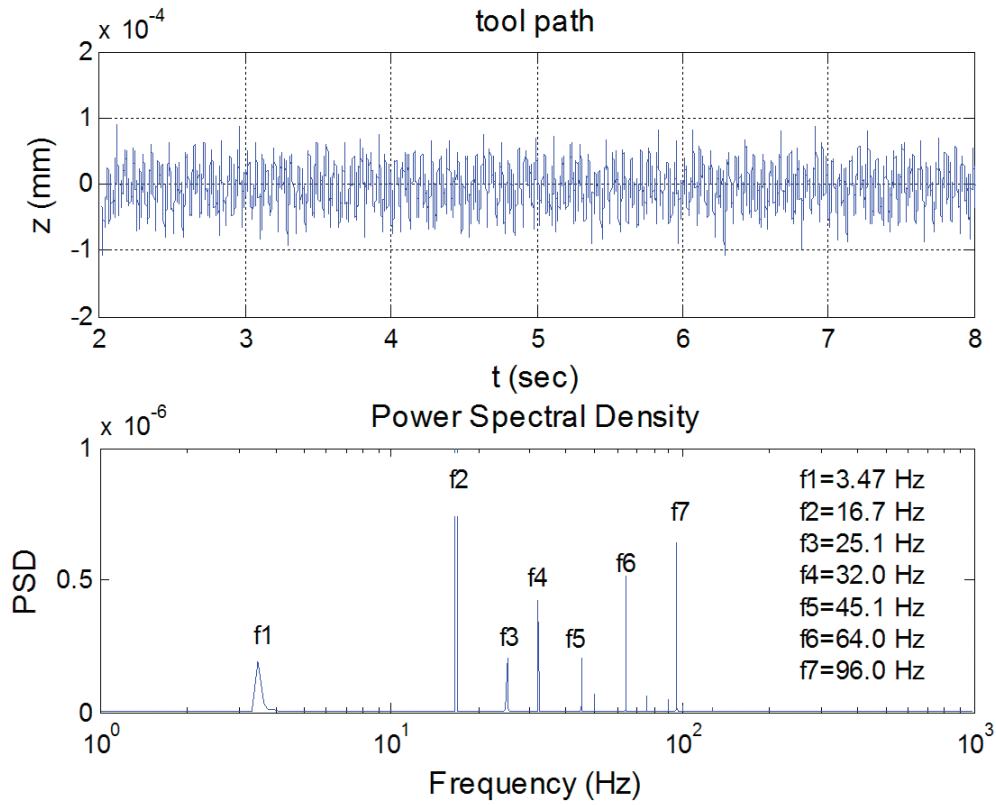
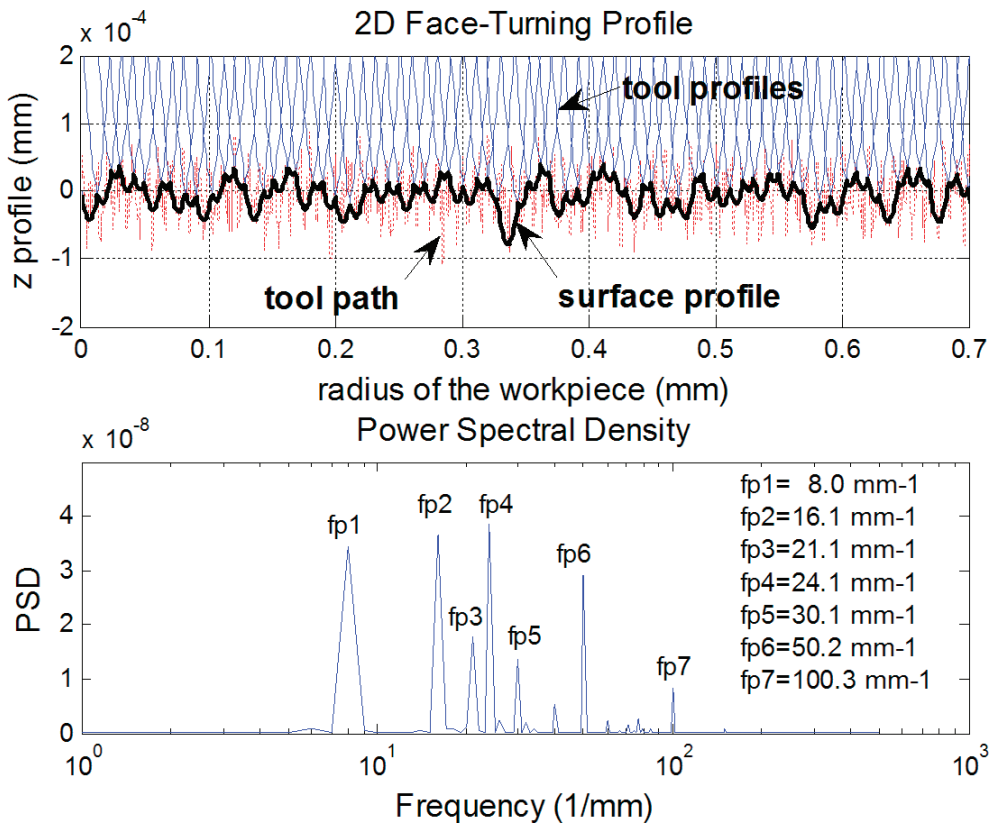**Fig. 12** Tool–workpiece relative displacement in the Z direction and its PSD

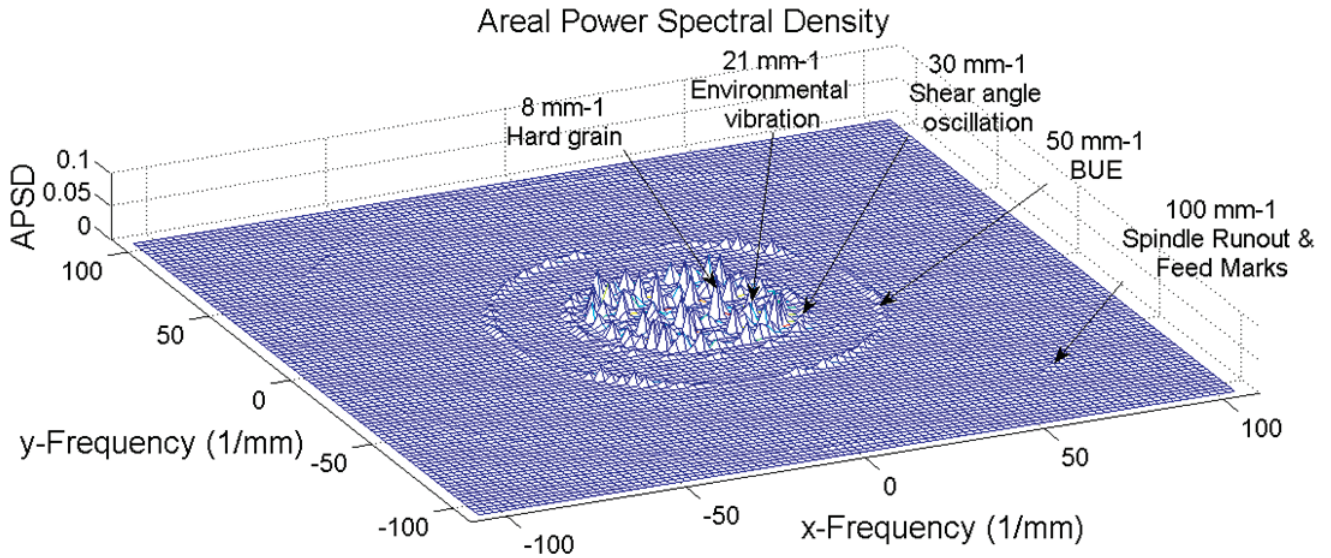**Fig. 13** Surface profile and its PSD

Fig. 14 Areal power spectral density of the simulated surface

In Fig. 10, there are two apparent counterclockwise flutes at the centre region of the surface. The wavelength of the flute is roughly 0.1–0.2 mm/cycle; in other words, the spatial frequency is 5–10 mm^{-1}. In APSD, four peaks on the ring of 8 mm^{-1} indicate that the two symmetrical pairs of flutes pass on the surface and leave the aliased spatial frequency with 8 mm^{-1}. As stated above, the spatial frequency of 192 mm^{-1} in the tool path is from the hard grain with the frequency assumed as 32 Hz.

The APSD bridges the gap between vibrations and the surface topography generation; the analysis reveals that the vibration contradicting the surface error is simply observed from the amplitudes. It is extremely efficacious to analyse the vibration source and shape details on the surface using the ASPD.

4.3 Significance of analysis on surface texture

Surface texture expresses the topography of a real surface composed of certain deviations from the ideal surface. Since the machined surface always contains the anisotropic flutes, the profile methods become invalid for the surface analysis. Comparatively speaking, it is more efficacious and impartial to employ the areal surface texture parameters to investigate the whole surface data on the evaluated surface area. For instance, the root mean square height of the surface S_q is one of the common roughness parameters (ISO/DIS 25178-2) being used

$$S_q = \sqrt{\frac{1}{M \times N} \sum_{j=1}^{N} \sum_{i=1}^{M} z^2(x_i, y_j)} \qquad (23)$$

**Table 3** Significance of dynamic factors on surface roughness

Factors		Sig_{qx} (%)
Workpiece material property	Hard grain	29.30
	Shear angle oscillation	7.39
Cutting process	BUE	12.67
	Regenerative vibration	6.63
	Tool wear	5.82
Machine tool performance	Slideway side stiffness	5.17
	Environmental vibration	9.86
	Spindle axial runout	3.74
Remainder		19.42

To quantitatively analyse the effects of the various factors on the surface generation, the surface texture significance Sig_{qx} is employed in the following formation

$$Sig_{qx} = \frac{|S_{qa} - S_{qx}|}{S_{qa}} \times 100\% \qquad (24)$$

Table 3 shows the significance of the main factors in the dynamic cutting process on surface roughness, based on the data listed in Table 2. The values illustrate that dynamic cutting factors have a high influence on the surface generation in the ultra-precision cutting process.

1. The discontinuity of materials makes a large contribution to the surface finish in nano/micro cutting. The most significant factors are caused by hard grain and shear angle oscillation. The
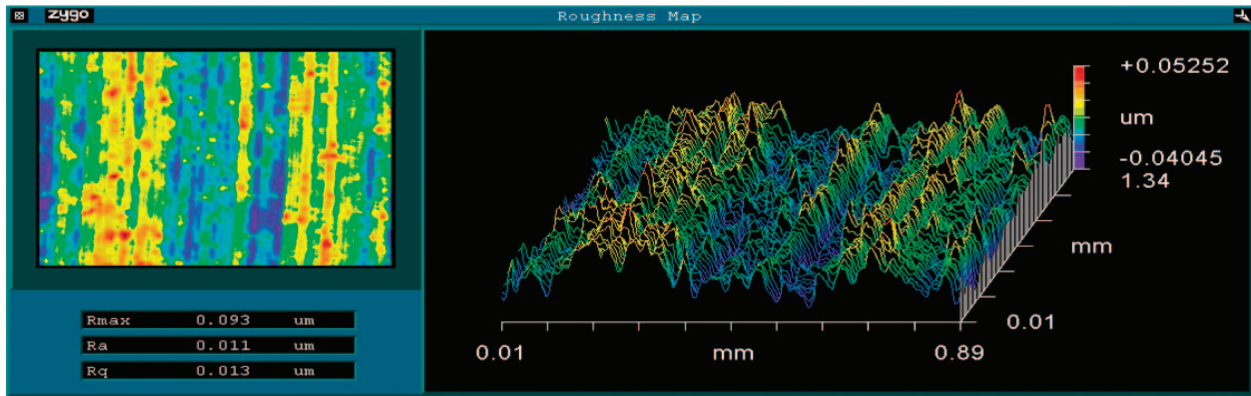
(a) Measurement of the machined surface
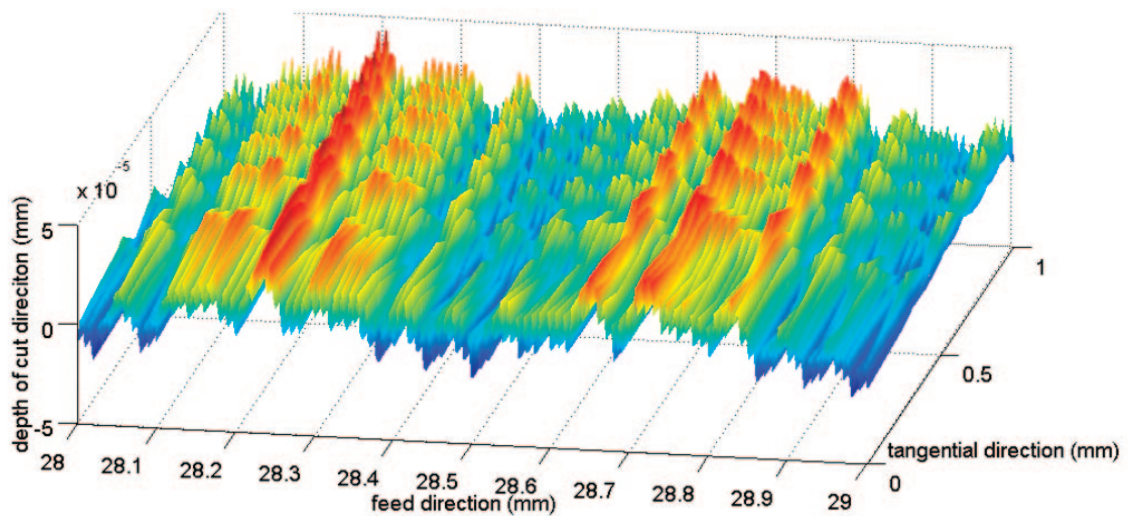
(b) Simulation of the machined surface

Fig. 15 Illustrative comparison of the machined and the simulated surface generated under the same cutting conditions

influences are clearly reflected in the PSD and APSD amplitudes. Especially the hard grain leads to the remarkable high-order harmonics in the cutting force and tool path, and thus composes the main surface texture. Applying the single crystal material is the most effective approach to improve the surface finish.

2. Cutting process dynamics is the second group to contribute to the surface texture. Coolant will help to reduce the BUE and tool wear, and the regenerative vibration can be suppressed by control of the previous residual height on the surface texture.

3. The interesting finding is that the spindle axial runout devotes even less than 4 per cent to the surface roughness. Comparing this with the PSD figure of the tool path and surface profile, it is concluded that the cause of the above result is the spindle runout being sharply attenuated by the 'sampling process'.

4. All the dynamics factors represent more than 80 per cent of the contributions to the surface roughness in terms of the significance. To improve the surface roughness in the system, it is recommended that the non-linear factors, such as adopting the homogeneous material and making the cutting system stiffer, especially for the dynamic response, should be tightly controlled.

5 EXPERIMENTAL VERIFICATION

In order to evaluate the effectiveness of the dynamic cutting process model and the surface prediction method, the surface simulated is verified through experimental work. Figure 15(a) shows the measurement result of an Al-6061 specimen which is machined at the conditions of 1000 r/min spindle speed, 0.01 mm/rev feedrate, 0.01 mm depth of cut, and 0.508 mm tool nose radius, measured using a

(a) APSD of the measured surface using Zygo 3D surface profiler

(b) APSD of the simulated surface
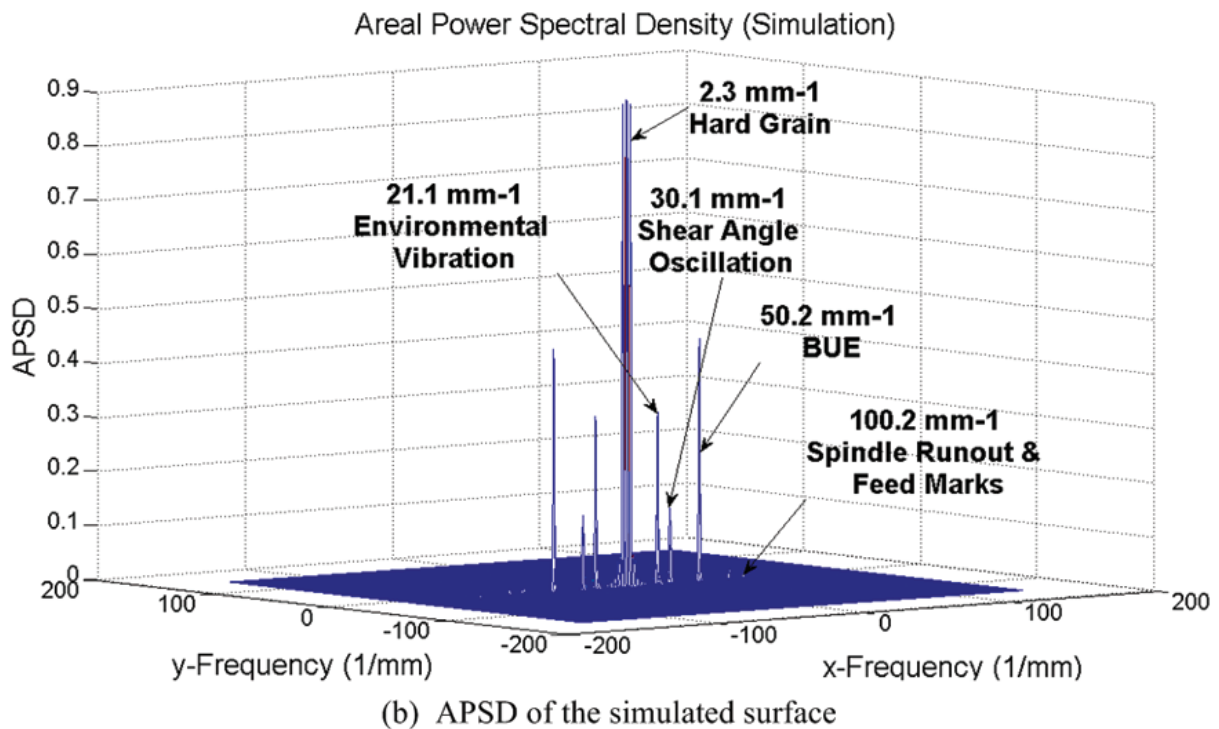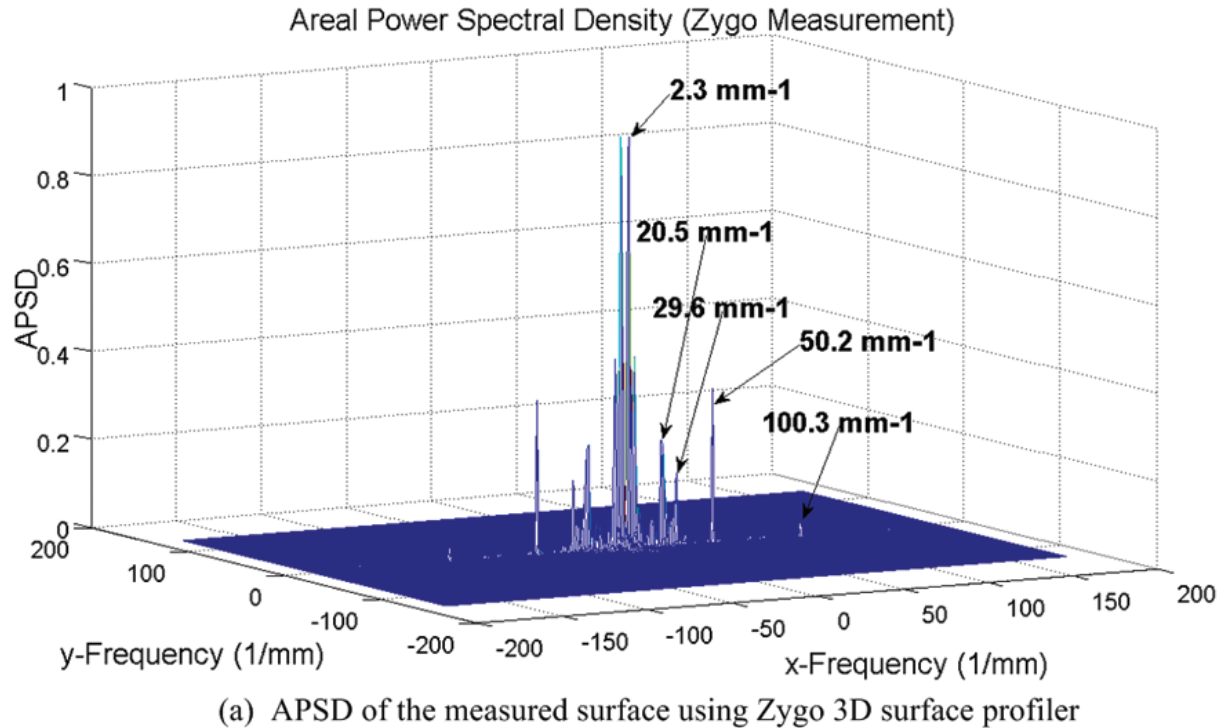
Fig. 16 APSD analysis on the machined and simulated surface

Zygo NV 5000 system. The measured surface locates at the 28–29 mm radius area where the tool marks are nearly in straight lines.

The machined surface is also simulated under the same cutting conditions as shown in Fig. 15(b). It is found that the form and features of the simulated surface are consistent with those of the machined surface. Different from the cutting at the axis centre, the hard grains turn to high frequency since the cutting speed at 28–29 mm radius is divided by the average grain size 30 μm. Its vibration on the surface profile is accordingly shifted to

$2.27\,\mathrm{mm}^{-1}$ after the sampling process by the spindle rotation.

To verify the modelling, simulation, and analysis method further, the sampled point data of the surface from Zygo measurements are processed by APSD, as shown in Fig. 16(a), and the corresponding APSD of the simulated surface, as shown in Fig. 16(b). The two APSD figures are identical and the relevant non-linear factor is highlighted in Fig. 16(b). The amplitudes of the APSD at certain frequencies also present the significances of the factors in the surface generation process, which also dovetail the significance analysis result, as discussed.

6 CONCLUSIONS

1. The nano/micro cutting process is combined with the material property, cutting chatter, tooling geometry, actuation servo capability, the machine mechanical structure, environmental vibrations, etc. The integrated simulation system can help to give a better understanding of the intrinsic relationship between the dynamic cutting process and the surface generation. The non-linear factors are included to emulate the real cutting conditions, such as hard grains of the material, BUE, regenerative vibration, tool wear, and spindle runout. Integrating the drive and control system with the cutting system modelling provides the flexibility to improve the control system performance and thus ultimately leads to the good surface quality that is desired.

2. The surface simulation algorithm should take account of the tool interference effect. The tool interference commonly appears when the low feed rate or big rake radius cutting tool is adopted. The tool interference may help to clear the higher remaining tool marks and generate the lower surface roughness rather than the poor surface finish.

3. Both the frequency ratio method and sampling theorem can interpret the surface topography formation. The spindle rotational frequency f_s samples the tool–workpiece relative vibrations to the aliasing frequencies as a lowpass filter. The components with frequencies higher than $f_s/2$ are attenuated sharply in one radial section profile.

4. The PSD method is effective for the component analysis in one radial section, while APSD is more powerful in both radial and circumferential directions. APSD provides vivid descriptions of the vibration frequencies, geometric distributions, and their amplitude proportions. From the APSD analysis, the original vibration in the tool path can be reconstructed.

5. Non-linear factors have a major effect on the nano/micro cutting process. The significance of non-linear factors in total is more than 80 per cent. The workpiece material heterogeneity is central to the surface roughness source. The fine-crystal material will positively lead to a better surface.

6. In the direct drive system, the force disturbances transmit into the tool–workpiece displacements through the servo motor and the slideway. Therefore, the Z axis servo performance and the slideway stiffness become the most critical parts in the dynamic cutting system. The higher the disturbance rejection, the better the surface quality becomes. The hydrostatic direct drive system can increase the physical stiffness and damping, and the higher gain in the velocity loop will enhance the damping, of the servo control system.

Currently, the authors are undertaking an optimization design of the machine structure and cutting conditions to improve the performance of the nano face turning process; the related experimental results will be presented in other papers in the near future. More studies on the well-designed cutting trials and simulations potentially applied to free-form surfaces in multiaxis nano/micro machining will be summarized in the authors' next study to further verify the approach developed.

REFERENCES

1 **Simoneau, A., Ng, E.,** and **Elbestawi, M. A.** Surface defects during microcutting. *Int. J. Mach. Tools Mf*, 2006, **46**, 1378–1387.
2 **Ni, H., Elmadagli, M.,** and **Alpas, A. T.** Mechanical properties and microstuctures of 1100 aluminum subjected to dry machining. *Mater. Sci. Engng*, 2004, **385**, 267–278.
3 **Cardi, A. A., Firpi, H. A., Bement, M. T.,** and **Liang, S. Y.** Workpiece dynamic analysis and prediction during chatter of turning process. *Mech. Systems and Signal Processing*, 2008, **22**(6), 1481–1494.
4 **Fang, N.** and **Dewhurst, P.** Slip-line modeling of built-up edge formation in machining. *Int. J. Mech. Sci.*, 2005, **47**, 1079–1098.

5 Durazo-Cardenas, I., Shore, P., Luo, X., Jacklin, T., Impey, S. A., and **Cox, A.** 3D characterisation of tool wear whilst diamond turning silicon. *Wear*, 2007, **262**, 340–349.

6 Jeong, G.-B., Kim, D. H., and **Jang, D. Y.** Real time monitoring and diagnosis system development in turning through measuring a roundness error based on three-point method. *Int. J. Mach. Tools Mf*, 2005, **45**, 1494–1503.

7 Cheung, C. F. and **Lee, W. B.** Characterisation of nanosurface generation in single-point diamond turning. *Int. J. Mach Tools Mf*, 2001, **41**, 851–875.

8 Cheung, C. F. and **Lee, W. B.** A theoretical and experimental investigation of surface roughness formation in ultra-precision diamond turning. *Int. J. Mach. Tools Mf*, 2000, **40**, 979–1002.

9 Cheung, C. F. and **Lee, W. B.** Modelling and simulation of surface topography in ultra-precision diamond turning. *Proc. Instn Mech. Engrs, Part B: J. Engineering Manufacture*, 2000, **214**(B6), 463–480.

10 Kim, D.-S., Chang, I.-C., and **Kim, S.-W.** Microscopic topographical analysis of tool vibration effects on diamond turned optical surfaces. *Precision Engng*, 2002, **26**, 168–174.

11 Lee, W. B. and **Cheung, C. F.** A dynamic surface topography model for the prediction of nano-surface generation in ultra-precision machining. *Int. J. Mech. Sci.*, 2001, **43**, 961–991.

12 Lee, W. B., Cheung, C. F., Li, J. G., To, S., Du, J. J., and **Yin, Z. Q.** Development of a virtual machining and inspection system for ultra-precision diamond turning. *Proc. IMechE, Part B: J. Engineering Manufacture*, 2007, **221**(B), 1153–1174.

13 Luo, X., Cheng, K., and **Ward, R.** The effects of machining process variables and tooling characterizations on the surface generation. *Int. J. Advd Mfg Technol.*, 2005, **25**(11–12), 1089–1097.

14 Luo, X. and **Cheng, K.** Nonlinear effects in precision machining of engineering materials. In Proceedings of the American Society of Precision Engineering Annual Meeting, Portland, Oregon, USA, 2003, pp. 489–493.

15 Takasu, S., Masuda, M., and **Nishiguchi, T.** Influence of study vibration with small amplitude upon surface roughness in diamond machining. *Ann. CIRP*, 1985, **34**, 463–467.

16 Delta Tau Data Systems, Inc. Turbo PMAC User Manual, 2006.

17 Childs, T. H. C., Maekawa, K., Obikawa, T., and **Yamane, Y.** *Metal cutting: theory and applications*, 2000, Arnold, London.

18 Schmidt, C., Frank, P., Weule, H., Schmidt, J., Yen, Y. C., and **Altan, T.** Tool wear prediction and verification in orthogonal cutting. In 6th CIRP International Workshop on *Modeling of machining operations*, Hamilton, Canada, 20, May 2003.

19 Yusuf Altintas *Manufacturing automation: metal cutting mechanics, machine tool vibrations, and CNC design*, 2000 Cambridge University Press, Cambridge.

20 Fan, X. and **Miller, M. H.** The application of an empirical tool force model on vibration assisted cutting. In Proceedings of the American Society of Precision Engineerings Annual Meeting, St Louis, Missouri, USA, 2002, pp. 484–489.

APPENDIX

Notation

a, b	integral and fractional part of the frequency ratio
A, B	constants in the tool wear process
A_{evx}, A_{evz}, f_{ev}	amplitude and frequency of the environmental vibration
A_{sr}, A_{sa}	amplitude of the spindle radial/axial runout
A_u, f_u	amplitude and frequency of the shear angle oscillation
AV	actual velocity
A_α, ω_α	amplitude and frequency of the rake angle variation due to the generation and removal of BUE
A_τ, A_H	incremental amplitude of the shear stress and hardness due to the hard grain
CV, CA	command velocity and acceleration
d_c	depth of cut
DAC$_{out}$	digital-to-analogue converter (DAC) output
e_{evx}, e_{evz}	environmental vibrations
e_{xz}, e_{zx}	errors of the slideways
e_{sr}, e_{sa}	spindle radial and axial runout
E	process activation energy
f	feed per revolution
f_p	new frequency spectrum emerging due to the sampling theorem
f_r	frequency ratio
f_s	spindle rotational frequency
f_v	vibration frequency in the time domain
f_{vs}	vibration frequency in the spatial domain
FE	following error
F_x, F_z	cutting force in the X/Z direction
F_r	resultant cutting force
h	undeformed chip thickness
H_t	hardness of the cutting tool material
IE	integral of the position error
K_{ff1}, K_{ff2}	cutting force coefficients at the flank face
K_p, K_i, K_d	proportional, integral, and derivative gains
K_{sp}, K_{sv}	position-loop and velocity-loop scale factors
K_{tc}, K_{rc}, K_{fc}	cutting force coefficients contributed by the shearing action in the cutting speed (tangential), normal (radial), and thrust (axial) directions respectively
K_{te}, K_{re}, K_{fe}	cutting force coefficients at the cutting edge in respective directions

K_{xz}, K_{zx} side-stiffness of X and Z slideways
K_{vff}, K_{aff} velocity and acceleration feedforward gains
l_w tool flank wear width
L_t projected length of tool edge in the X direction
m cycles of the spindle rotation lost in the sampling
min   function to return the smallest element
n spindle speed
N_p total simulation points
N_r total number of the spindle rounds in machining
N_s total number of sections
Pul   signal generator of pulse at regular intervals
R universal gas constant
R_w workpiece dimension
R_0 tool nose radius
S_q root mean square height of the surface
S_{qa} surface roughness S_q when all the factors are active in the simulation
S_{qx} surface roughness S_q when only the factor x is switched off in the simulation
Saw   signal generator of the sawtooth wave
Sig_{qx} surface texture significance of x factors on the surface roughness S_q
T spindle revolution period
T_f cutting temperature in the tool flank zone

V, V_s cutting speed and sliding speed
x, y, z remained tool profile points in the rectangular coordinate
x_c, y_c, z_c tool nose points in the rectangular coordinate
x_{sm}, z_{sm} servo motions of X and Z slideways
x_{tp}, z_{tp} real tool path in the machine tool coordinate system
β side clearance angle
$\Delta c_t, \Delta c_w$ variation of cutting thickness and cutting width
Δf tool profile spacing
Δu change of the shear angle from oscillation
$\Delta \alpha$ variation of the rake angle due to BUE
$\Delta \theta$ simulated angular spacing
$\Delta \tau, \Delta H$ increment of the shear stress and hardness due to the hard grain
θ, r, h remaining tool profile points in the polar coordinate
θ_a, r_a, h_a tool nose points in the polar coordinate
θ_r intersection angle of two continuous tool paths
θ_t, r_t, h_t all tool profile points in the polar coordinate
μ friction angle coefficient
ω, ϕ_r, ϕ_a spindle angular speed and phase shift of radial/axial runout